phys. stat. sol. (b) **245**, No. 6, 1033–1040 (2008) / **DOI** 10.1002/pssb.200777601

physica status solidi b
www.pss-b.com
basic solid state physics

Optical spectroscopy of single-walled carbon nanotubes: From excitonic effects towards control of the radiative lifetime

Robert Pomraenke, Parinda Vasa, and Christoph Lienau*

Institut für Physik, Carl von Ossietzky Universtität Oldenburg, 26111 Oldenburg, Germany

Received 10 September 2007, revised 21 September 2007, accepted 10 March 2008
Published online 30 April 2008

PACS 42.65.Re, 71.35.–y, 73.22.–f, 78.47.Cd, 78.67.Ch

* Corresponding author: e-mail christoph.lienau@uni-oldenburg.de, Phone: +49-441-7983485, Fax: +49-441-7983890

We have recently studied excitonic effects on the optical properties of single-walled carbon nanotubes by means of two-photon spectroscopy and time-resolved photoluminescence spectroscopy. For nanotubes with diameters between 6.8 Å and 9.0 Å, the two-photon spectra give evidence for large binding energies between 300 meV to 400 meV. Theoretical simulations of these spectra indicate that the lowest energy exciton state in nanotubes is an optically dark exciton, which has profound implications on the luminescence yield and exciton dynamics in single-walled nanotubes. Indeed, time-resolved photoluminescence measurements of individual nanotubes reveal low quantum yields and rather short exciton lifetimes ranging from 10 ps to 200 ps, which are affected by exciton relaxation between bright and dark states and non-radiative exciton recombination. These results suggest that a control of the radiative lifetime of nanotube excitons may be a viable strategy for enhancing their luminescence yield. Here, we propose that exciton-coupling to surface plasmon polaritons in metallic nanostructures may result in a substantial enhancement of the radiative exciton decay rate.

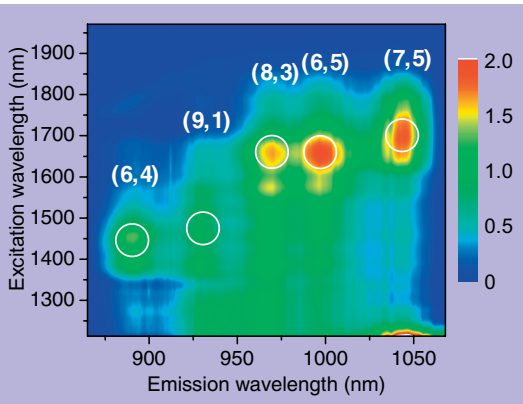

Two-photon luminescence excitation spectra of single-walled carbon nanotubes. The luminescence intensity is plotted as a function of excitation and detection wavelength. The various two-photon resonances are assigned to nanotube species with different chiral indices (n,m), as indicated in the figure.

1 Introduction In single-walled carbon nanotubes (SWNT) electron and hole wavefunctions are strongly quantum-confined to the circumference of a cylindrical tube with a diameter in the range of 1 nm and a length of up to several millimeters. This makes SWNT – at least conceptually – interesting model systems for exploring the effects of the Coulomb interaction between electron and hole on the optical properties of quasi-one-dimensional quantum systems. Indeed, we have witnessed an upsurge of interest in the excitonic properties of SWNT during the last few years [1].

Although initial attempts were made to interpret the optical spectra in terms of a single-particle excitations [2] governed by the van-Hove singularities in the density of states of a quasi-one-dimensional system, it has soon been realized that excitonic effects are particularly strong for SWNT. In 2004, different groups reported theoretical investigations of the transition frequencies and the shape of optical SWNT spectra in the presence of Coulomb correlations [3–7]. One year later, two-photon-induced photoluminescence experiments [8, 10] gave convincing evidence that the exciton binding energies in SWNT are indeed large

and correspond to a significant fraction of the band gap. Since then, a variety of detailed experimental and theoretical studies have greatly improved the understanding of these properties [9–17].

In the first part of this paper, we give a brief review of our experimental and theoretical results. Specifically, two-photon-induced luminescence experiments [8], giving evidence for large exciton binding energies of 300 meV to 400 meV for nanotubes with diameters between 6.8 Å and 9.0 Å, are discussed. The theoretical analysis of these results indicates that the lowest energy SWNT exciton state is an optically dark triplet state. This finding is in agreement with various other recent observations [6, 15, 17, 18] and explains the low fluorescence quantum yield as well as the comparatively short exciton lifetime in the 10–100 ps range [19], which are much shorter than the expected radiative lifetime observed even for an individual SWNT [21].

This low fluorescence yield is a limiting factor for applications of nanotubes in various optoelectronic devices and its enhancement would be highly desirable. It thus appears relevant to search for novel ways to enhance this yield. One recently explored strategy is to use high magnetic fields to mix bright and dark exciton states [17]. Another possible approach consists in reducing the spontaneous exciton emission rate, e.g., by coupling to surface plasmon polariton (SPP) excitations in metallic nanostructures. SPP excitations in metallic structures are promising because they carry the potential to localize visible light down to the 10 nm regime or even beyond [22] and because they are known to exhibit strong radiative damping [23]. This makes it likely that the interaction between excitons and localized SPP modes can profoundly alter the spontaneous emission properties of excitons. However, little is known about such interactions so far. Here, we report on a preliminary study of an interesting prototype system consisting of a nanometer-sized array of metallic slits deposited on a semiconductor quantum well. Angle-resolved reflectivity spectra at low temperature reveal a significant coupling between quantum well excitons and surface plasmon polariton excitations of the metal grating.

2 Two-photon-induced luminescence spectroscopy of single-walled carbon nanotubes The idea behind comparing linear and nonlinear optical spectra is to make use of the different symmetry selection rules for one- and two-photon photoluminescence to specifically address excitonic states having different symmetries. In carbon nanotubes, one expects that for each allowed interband transition there exist a series of transitions to optically active exciton states having odd (u) symmetry with respect to rotations by π about the nanotube *U*-axis [8, 24, 25]. Two-photon spectroscopy, on the other hand, couples to the otherwise optically inactive even (g) states. The energetic splitting between the one- and two-photon active states is proportional to the exciton binding energy.

Experimentally, we use 100 fs laser pulses from a Ti:sapphire oscillator, operating at a repetition rate of 80 MHz and tunable between 700 nm and 970 nm for one-photon-excitation. The Ti:sapphire laser also pumps an optical parametric oscillator, delivering sub 150 fs pulses at 80 MHz repetition rate in the wavelength range between 1150 nm and 2000 nm. For two-photon spectroscopy, these pulses are focussed to a spot size of about 3 µm into a solution of single-walled carbon nanotubes suspended in D_2O with sodium dodecyl sulfate as surfactant. The tubes were produced by the HiPCO method. Photoluminescence from the sample was collected in a 90° configuration using a second microscope objective, spectrally dispersed in a 0.5 m monochromator and detected with a liquid nitrogen cooled charge coupled (CCD) device. All experiments are performed at room temperature.

Typical photoluminescence spectra recorded with this setup for one-photon excitation at 800 nm show the emission from 6 different nanotube species [(6,4), (9,1), (8,3), (6,5), (7,5) and (9,4)] in the wavelength range between 850 nm and 1150 nm accessible with the silicon-based CCD detector. The assignment of the chiral indices (n_1,n_2) of these tubes is based on previous Raman [26] and luminescence [2] data.

Spectrally-resolved two-photon luminescence excitation spectra of our sample for below band gap excitation between 1210 nm and 1970 nm are shown in the Titlefigure. In these experiments, the excitation wavelength was changed in 5 nm steps by tuning the optical parametric oscillator. For each excitation wavelength the laser power is kept constant at 60 mW, corresponding to an excitation intensity of about 30 GW/cm^2 and the photoluminescence spectrum was integrated over 60 seconds. The different tube species are readily identified via their characteristic emission wavelength and the chiral indices are assigned as

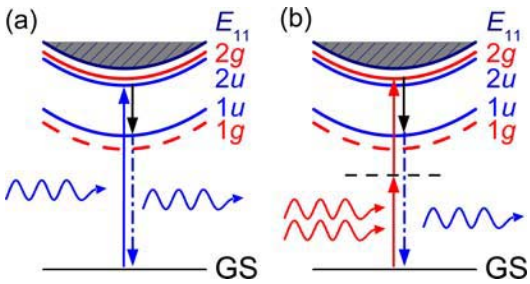

Figure 1 (online colour at: www.pss-b.com) Schematic of absorption and emission processes in carbon nanotubes via (a) one photon and (b) two-photon transitions. E_{11} indicates the single-particle transition between the lowest subbands. One-photon excitations (solid blue line) couple to excitonic states with odd (u) symmetry with respect to π rotations about the *U*-axis. The *U*-axis is perpendicular to the tube axis through the center of the C hexagons [24]. (1) and (2) indicate the symmetry of the envelope function with respect to reflection in the $z = 0$ plane. Two-photon excitations (solid red lines) couple to the 2g exciton state. Exciton relaxation into the 1u state is indicated by a black solid line and photon emission from the 1u state by a blue dash-dotted line.

indicated above. The important observation is that – for each tube – one finds a maximum in the luminescence intensity at an excitation wavelength that is far above the emission wavelength, but significantly smaller than twice the emission wavelength. These absorption maxima are assigned to resonant two-photon excitation of the lowest two-photon allowed exciton state (2g) [8]. The positions of the maxima thus correspond to half the energy of these allowed states. Emission results from relaxation into the lowest one-photon active 1u state (Fig. 1). The large shift of about 240–320 meV between both states is a signature of (i) the excitonic nature of absorption and emission at room temperature and (ii) exciton binding energies of almost one fourth of the band-gap energy.

In Fig. 2, we directly compare one- and two-photon spectra for the (7,5) nanotube, emitting at 1045 nm. In these spectra, the emission intensity is plotted as a function of the excess energy, i.e, $E^{ex} - E_{11}^{1u} = \hbar\omega - E_{11}^{1u}$ for one-photon, and $2\hbar\omega - E_{11}^{1u}$ for two-photon excitation, respectively. The two-photon spectrum simply shows a single resonance, roughly 240 meV above the luminescent state. Similar spectra and splittings (between 240 meV and 325 meV) are also found for the other investigated nanotubes species and are in agreement with other recent two-photon results [10, 11].

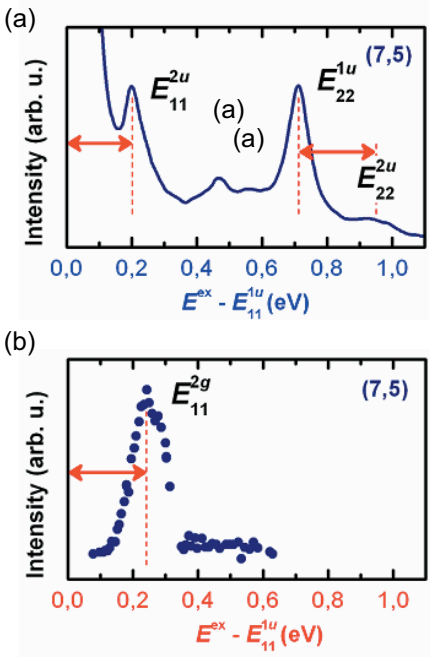

Figure 2 (online colour at: www.pss-b.com) Comparison of (a) one-photon and (b) two-photon luminescence excitation spectra of the (7,5) tube emitting at 1045 ± 5 nm. The abscissa gives the difference between the absorption and emission energy. For one-photon absorption, E_{11} and E_{22} indicate the first- and second-subband transitions, respectively. The peak at 0.2 eV is assigned to the 2u exciton resonance. In two-photon absorption, the 2g state is excited at 0.24 eV above the 1u emission, pointing to an exciton binding energy of about 300 meV.

For a quantitative interpretation the experimental results are compared to a detailed theoretical modelling of the nanotube optical spectra. Obviously such a modelling is rather challenging and only recently appropriate theoretical methods have been developed. We use the approach reported in Ref. [3], starting from single-particle wavefunctions obtained by density functional theory in GW approximation. The optical properties are then calculated by solving the Bethe-Salpeter Eq. (BSE) for the two-particle electron–hole excitations. This approach gives energies and wavefunctions of the relevant excitonic states including their optical selection rules.

Calculated one- and two-photon absorption spectra for the (6,4) tube are shown in Fig. 3. In the absence of Coulomb interaction, both one- and two-photon spectra show peaks at an energy corresponding to the difference between the lowest nanotube subband in the conduction and valence band, E_{11}. In the one-photon spectrum, the spectral shape reflects the one-dimensional density of states, apart from the finite broadening of the spectrum of 100 meV, which has been included phenomenologically in order to account for both homogeneous and inhomogeneous broadening in the experimental spectra. Switching on the electron–hole interaction shifts the lowest one-photon active transition strongly to the red, indicating an exciton binding energy of 0.54 eV. The shape of this spectrum reflects the excitonic density of states and their broadening. Due to the strong Coulomb correlation, the contribution of the free carrier continuum vanishes almost completely and is thus difficult to observe experimentally. In agreement with the experiment, the two-photon spectrum essentially shows a single resonance, 380 meV above the lowest one-photon active resonance, and below the E_{11} energy.

The theoretical calculations not only provide a quantitative description of our experimental results but also allows us to analyze the relevant exciton states in more detail. We find four optically relevant bound exciton states below the single-particle gap (dashed gray line at an energy of 0.5 eV in Fig. 3), with binding energies of 0.54 (1g), 0.50 (1u), 0.16 (2g) and 0.16 eV (2u). Here, the binding energy is taken as the energy difference between the most strongly bound exciton state and the onset of the single-particle continuum.

The fact that these four states fall into two different energy groups, the (1g, 1u) and (2g, 2u) states, can readily be understood by considering that the electron and hole wavefunctions are quantum-confined to the circumference of a small cylinder having a diameter of only about 1 nm. For such a case, under the influence of the Coulomb interaction, the Schrödinger equation predicts that the lowest energy exciton state (1) will have a symmetric exciton relative wavefunction, approximately given as $\psi_1(z;a) = \exp(-a|z|)$, which is localized along the axis and essentially fully delocalized along the circumference of the tube. The next higher bound exciton state (2) then has an antisymmetric relative wavefunction, $\psi_2(z;b) \simeq z\exp(-b|z|)$, which is more delocalized along the tube axis. This is in-

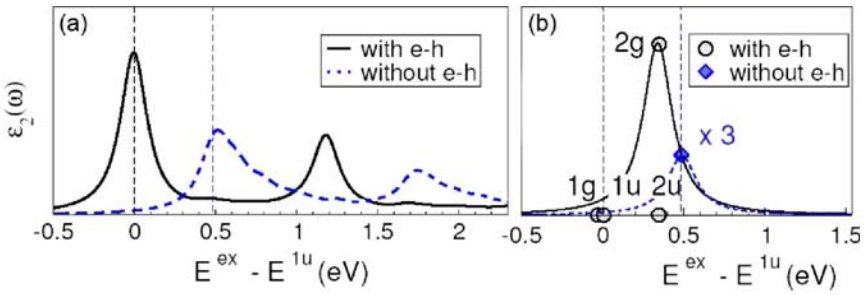

Figure 3 (online colour at: www.pss-b.com) *Ab-initio*-calculated (a) one-photon and (b) two-photon absorption for the (6,4) tube with a Lorentzian broadening of 0.1 eV. Black (blue dashed) lines are with (without) electron–hole (e–h) interactions. The black circles in two-photon absorption denote the probability amplitude for two-photon scattering to the exciton states 1g, 1u , 2u, and 2g. The probability amplitude of scattering to the final state without e–h interaction is indicated by a blue diamond.

deed quite well confirmed by the full *ab-initio* calculations. The lowest energy exciton wavefunctions (1g, 1u) extend over several nm along the tube axis and is delocalized along the circumference [Fig. 4(a))]. The higher exciton states (2g, 2u) are more extended along the tube axis and have a nodal plane at $z = 0$, see Fig. 4(b). Thus, the calculated wavefunctions are indeed Wannier-like and are only weakly dependent on the circumference direction.

The *ab-initio* calculations give the *local* electron density for each atom and not just the relative wavefunction of the exciton as in a more conventional continuum model. A zoom into these wavefunctions is displayed in Fig. 4(c). The four panels display the amplitude of the electron wavefunction when the hole is placed in the center of the bond at $z = 0$. Their parity under rotation about the *U*-axis governs the optical dipole selection rules in carbon nanotubes. The u states are one-photon active, whereas g states are two-photon allowed.

These results thus suggest that the 1u exciton state dominates the one-photon absorption spectra of carbon

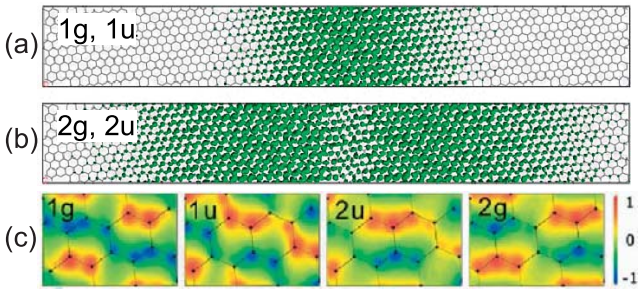

Figure 4 (online colour at: www.pss-b.com) Lowest-energy excitonic wave functions for the (6,4) tube from *ab-initio* calculations. The panels (a) and (b) correspond to the 1g, 1u and 2g, 2u states, respectively, and show the probability of finding the electron on the tube surface when the hole is fixed at the center of the panel $z = 0$. The vertical direction corresponds to the circumference (2.1 nm) and the horizontal direction with a length of 15.9 nm to the tube axis. The bottom four panels (c) are blowups of the same states. They display the wave-function amplitude of the electron when the hole is placed in the center of the bond at $z = 0$ and show the parity under rotation by 180° about the *U*-axis. The linear color scale is in arbitrary units.

nanotubes. This state, however, is not the most lowest energy state. The most strongly bound exciton state is the 1g state which, however, is optically inactive in one-photon absorption and, according to the calculations, contributes weakly in two-photon absorption [6]. Thus, the theoretical calculations suggest that the optical excitation of the exciton resonance dominates the experimental two-photon luminescence spectra. From the energy splitting between 2g and 1u states, the exciton binding energy can thus be derived provided that an appropriate model for the Coulomb interaction is used. Our calculations suggest exciton binding energies of about 250 meV for the (7,5) tube and about 320 meV for the (6,4) tube.

An important result of these *ab-initio* calculations is the finding of an optically inactive, dark exciton state, denoted as 1g, energetically slightly below the lowest optically active 1u state. The existence of such dark exciton states has already been discussed earlier based on semiempirical models [6]. Such low-lying dark states may have a pronounced effect on the exciton dynamics and in particular the luminescence quantum yield of nanotubes, as excitons in the optically bright 1u state can relax into such a dark state and may get trapped at sufficiently low temperature, which may lead to a predominantly non-radiative decay rather than a radiative exciton decay.

Indeed, early time-resolved measurement on nanotube ensembles showed exceedingly short luminescence lifetimes in the 10 ps range and low quantum yields of typically less than 10^{-3} [19, 20]. Temperature-dependent time-resolved PL measurements on individual SWNT [21] revealed pronounced fluctuations in the PL lifetimes, varying between about 20 ps and 200 ps at 87 K. The temperature dependence of the PL lifetime observed for an individual nanotube, showing a *decrease* in PL lifetime from about 100 ps at around 50 K to 20 ps at 200 K, was in marked contrast to the $\sqrt{T}$ *increase* with increasing temperature expected for a radiatively decaying quasi-one-dimensional quantum system. These measurements gave evidence for a thermally activated nonradiative decay of the exciton population. The fluctuations in the lifetimes suggested that extrinsic nonradiative decay channels, i.e., trapping into defect states dominates the PL decay of most of the tubes. The observation of rather

short, sub-ps, decay times for all tubes, however, pointed to the presence of an intrinsic nonradiative decay channel, e.g., trapping into dark exciton states, which is important at least at low temperatures. Recently, detailed temperature-dependent ensemble studies of both the quantum yield and the decay rate suggested that the intrinsic exciton decay is indeed governed by a statistical mixture of thermally equilibrated exciton populations in optically dark and bright states. The results suggest that the energetic splitting between dark and bright states is rather small (a few meV). Therefore, the dark states mainly affect the low temperature decay, whereas the fast exciton decay at room temperature is mostly governed by external nonradiative decay channels.

3 Exciton – surface plasmon polariton interaction in hybrid metal–semiconductor nanostructures It is apparent from all these studies that the luminescence yield from an individual SWNT is rather low, particularly at room temperature, and that nonradiative channels play an important role for the exciton decay. This low luminescence yield is of course a limiting factor for various applications of SWNT in optoelectronic devices. Different possibilities may exist to artificially enhance the luminescence yield. One possible approach consists in affecting the energetic ordering of the dark and bright states and/or inducing a mixing of those states, e.g., by applying external electric or magnetic fields. In fact, an enhancement of the low-temperature luminescence yield has been achieved recently by mixing dark and bright states in – rather large – external magnetic fields [17].

A very different strategy which does not necessarily require large external fields may consist in tailoring the radiative damping rate k_{rad} of the nanotube excitons, leading to an enhancement of the luminescence yield $\eta = k_{rad}/(k_{rad} + k_{nr})$, with k_{nr} being the nonradiative decay rate. Such an enhancement of the spontaneous emission rate, achieved by enhancing the local electromagnetic field density in the vicinity of the emitter, has been succesfully achieved for, e.g., quantum dots coupled to micropillars or defect modes of photonic crystals. In these configurations, the strong coupling regime has recently been reached. An alternative approach towards localizing electromagnetic fields uses metallic nanostructures, in which the interference of surface plasmon polarizations can result in field localization down to a scale of 10 nm or even below. This strong field localization led to the demonstration of various interesting phenomena such as Surface Enhanced Raman Scattering [27], enhanced transmission through metallic nanohole arrays [28] or ultrafast tip-enhanced electron emission [29]. A drawback of such metallic nanoresonators are of course the rather low quality factors due to the optical losses in the metal. So far, quality factors of at the most a few hundred have been achieved [30]. At present, there is only very limited information available about how field localization in metallic nanostructures affects the optical properties of quantum emitters.

Here, we propose to study metal nanoslit arrays deposited on semiconductor quantum well structures as prototypical system for investigating exciton – surface plasmon polariton coupling in hybrid systems. Some of the most important reasons for choosing such a structure are that (i) nanoslit arrays with slit widths in the 20–100 nm range can now be fabricated with high precision using electron beam lithography or focussed ion beam milling, (ii) the optical properties of nanoslit arrays deposited on passive dielectric substrates have recently been studied in some detail [30–33] and (iii) quantum wells, when optically pumped, provide high gain coefficients which may be sufficient to significantly reduce SPP damping due to Ohmic losses in the metal and potentially even reach surface plasmon polariton lasing. From the above-cited studies and others it is now understood that such metal nanoslit arrays with grating periodicities in the range of one micron show quite large transmission coefficients at certain resonance wavelengths, connected to SPP excitation at either the metal/air or metal/dielectric interface. The transmission coefficients are particularly large because of a propagating waveguide mode inside the nanoslits which exists even for vanishing slit widths. This allows one to reach significant

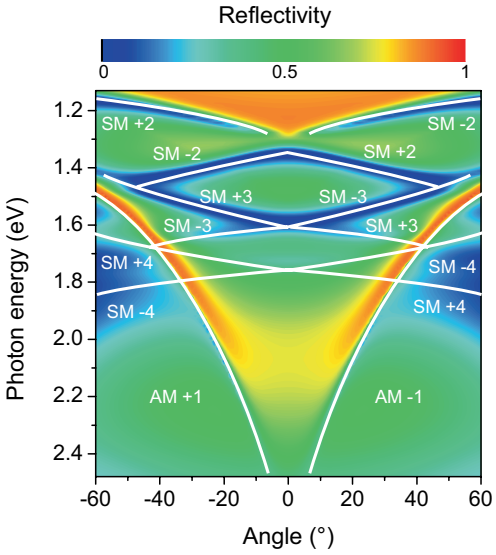

Figure 5 (online colour at: www.pss-b.com) Calculated zero-order angle-resolved linear reflectivity spectra of a hybrid metal semiconductor plasmonic crystal consisting of a gold nanoslit array deposited on a bulk semiconductor. The dispersion relation for different Air–Metal (AM) and Semiconductor–Metal (SM) surface plasmon polariton (SPP) resonances, i.e., the band structure of the hybrid crystal, is reflected in these spectra due to the grating coupling induced by the slit array. The grating parameters used for this calculation are: period $a = 490$ nm, height $h = 80$ nm and slit width $d = 130$ nm. The refractive index of the semiconductor n_S is chosen as 3.66 to be close to that of gallium arsenide. p-polarized incident light is assumed. The white lines serve as a guide to the eye and indicate the idealized SPP dispersions, neglecting SPP interactions.

field enhancement inside and near the nanoslits and to couple light to rather long-lived SPP excitations with lifetimes of up to several hundred femtoseconds [30].

When deposited on a semiconductor, e.g. a Gallium arsenide layer, the angle-dependent reflectivity and transmission spectra of such nanoslit arrays are markedly affected by the high refractive index of the semiconductor. This is illustrated in Fig. 5 showing simulated angle-dependent reflectivity spectra of a gold nanoslit grating with a period a of 490 nm, height h of 80 nm and slit width d of 130 nm. The refractive index n_S of the semiconductor layer below the grating is chosen as 3.66 to be close to that of Gallium arsenide. The simulations are performed for linearly p-polarized monochromatic plane light waves incident at angle θ with respect to the grating normal. The calculations are based on a diffraction model employing approximate surface impedance boundary conditions at the interfaces [33, 34]. This model has been used quite successfully to interpret earlier experimental results [30–32]. The resonances in the reflection spectra arise from grating coupling to SPP modes at either the air/metal (AM) or semiconductor/metal interface. Depending on the diffraction order p, the in-plane SPP wave vector is given as $k_{SP} = k_{||} + p \cdot 2\pi/a$, with $k_{||} = (\omega/c)\sin(\theta)$ being the in-plane wave vector of the incident light. The resonances are thus labeled as AM [p] and SM [p] for excitation of SPP modes at the air and semiconductor side of the metallic film, respectively. The white lines in Fig. 5 illustrate schematically the dispersion relation of the different resonances in the absence of interactions.

The spectra in Fig. 5 indicate that at energies of 1.5 eV, i.e., around the lowest exciton resonance of a typical 10 nm GaAs quantum well, and at angles of incidence around 40°, three different SPP modes, the AM [–1], SM [+2] and SM [–3] mode, are almost in resonances. Thus one may anticipate that in this energy and angular range, the AM [–1] SPP mode at the air/metal interface is efficiently coupled to the SM [+2] and SM [–3] modes at the semiconductor side of the metal film. This coupling is mediated via the propagating waveguide mode inside the nanoslits, which is indeed verified by calculating the electromagnetic mode profiles of this nanoslit structure in this range of energies and angles of incidence.

The spatial distribution of the tangential magnetic field H_y under illumination with a plane p-polarized monochromatic light wave with an energy of $E = 1.517$ eV, incident at an angle $\theta = 38°$, is shown in Fig. 6. The incidence conditions were chosen to give significant coupling between SM [–3], SM [+2] and AM [–1] SPP resonances. The calculations indeed show the formation of such a coupled mode, with a high field intensity inside the nanoslits and spatially localized field intensities at both the metal/air and metal/semiconductor interfaces. The fields at the semiconductor side are mostly evanescent in nature and decay within the first 50 nm from the interface. The fields at the air side contain both evanescent and propagating components and thus couple strongly to the zero-order far-field radiation. Thus under these conditions, light incident from the air side is efficiently coupled via the nanoslits into the semiconductor material and then rescattered into propagating far-field radiation on the air-side of the interface. Therefore, one may expect that such a field distribution is sensitive to an optical coupling to the excitonic resonance of a semiconductor quantum well, provided that it is placed close to the metal, within the decay length of the evanescent field inside the semiconductor.

Based on these considerations, we have designed a multilayer metal–semiconductor hybrid structure illustrated in Fig. 7(a). It consists of a 10 nm GaAs quantum well (QW) layer embedded in $Al_{0.3}Ga_{0.7}As$ barriers deposited on a GaAs substrate. On the top side, the AlGaAs barrier has a height of only 20 nm and is capped by a 3 nm GaAs buffer to ensure that the QW is close to the metal while maintaining sufficient optical quality. On top of this QW, a 80 nm thick Gold film is deposited and a grating structure with a period of 490 nm and a slit width of 130 nm is fabricated by electron beam lithography. A scanning electron microscope image of the grating is shown in Fig. 7(b). Photo-luminescence studies indicate the effect of the grating fabrication on the optical properties of the QW is negligible.

The optical properties of this hybrid structure have been investigated by linear low-temperature angle-resolved reflectance spectroscopy. Monochromatic p-polarized light from a tunable Ti:sapphire laser is weakly focused to a

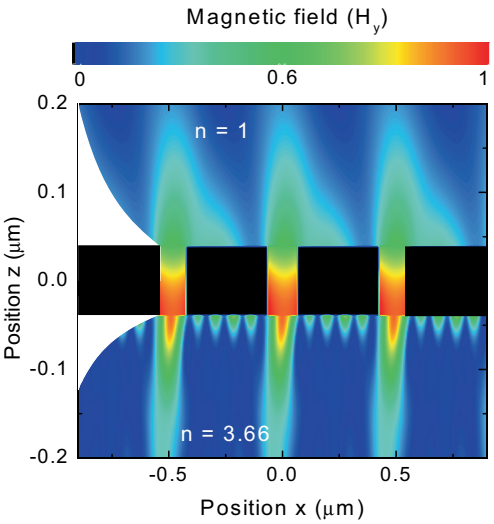

Figure 6 (online colour at: www.pss-b.com) Calculated spatial distribution of the tangential magnetic field H_y near the crossings of the SM [+2], SM [–3] and AM [–1] SPP resonances in Fig. 5, i.e, for illumination with a plane p-polarized monochromatic light wave with energy $E = 1.517$ eV and angle of incidence $\theta = 38°$. The calculations show the formation of a strongly radiatively damped, optically bright mode in which the magnetic field is spatially localized at the slits. The spatial overlap of SPP field and QW near the slits is expected to cause a finite optical coupling between SPPs and excitons. The exponential decay of the field profiles along the z-direction is also schematically indicated.

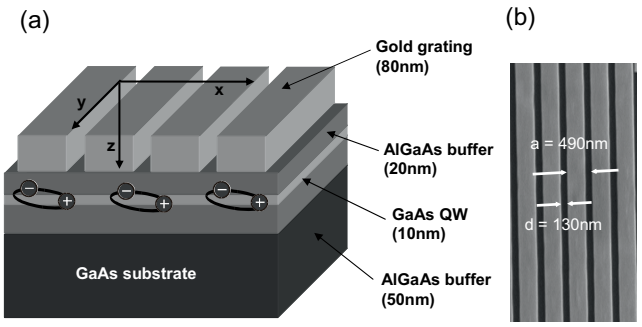

Figure 7 (online colour at: www.pss-b.com) (a) Schematic of the multilayer metal–semiconductor hybrid structure consisting of a gold grating and a GaAs/AlGaAs quantum well. As seen from Fig. 6, a comparatively large slit width of $d = 130$ nm was chosen to provide a significant overlap between localized SPP modes and QW. (b) Scanning electron micrograph of the sample surface showing the metal grating with period $a = 490$ nm and a slit width $d = 130$ nm. The height of the grating is $h = 80$ nm.

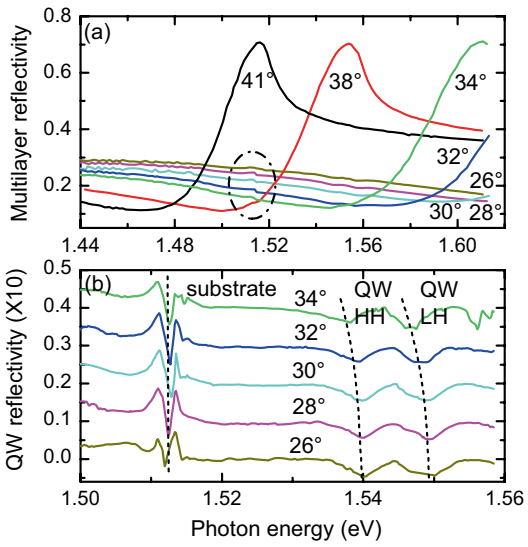

Figure 8 (online colour at: www.pss-b.com) (a) Experimentally measured angle-resolved reflectivity spectra of the multilayer metal–semiconductor hybrid structure described in Fig. 7. The data were recorded at a temperature of 10 K and are dominated by the reflectivity peak of the SPP resonance resulting from the coupling between the AM [–1], SM [+2] and SM [–3] modes. In these overview spectra, only faint features from the QW and substrate resonances are observable. (b) Higher resolution low-temperature reflectivity spectra of the multilayer metal–semiconductor hybrid structure for different angles close to the SPP–exciton crossing obtained after subtracting the SPP contribution. The spectra reveal a clear spectral shift of the Heavy-Hole (HH) and Light-Hole (LH) QW resonances.

spot size of about 200 μm onto the grating structure. The angle θ of the incident light is varied in a computer-controlled setup with a step size down to 0.1° and the reflected light is recorded with a balanced photodiode. Representative overview spectra in the energy range between 1.44 eV and 1.62 eV and for angles of incidence between 26° and 34° are shown in Fig. 8(a). The data are recorded at a sample temperature of 10 K and are dominated by the strong reflectivity peak of the SPP resonance resulting from the coupling between the AM [–1], SM [+2] and SM[–3] modes. As expected from Fig. 5, the energetic position of the SPP resonance shifts strongly with incidence angle. In these overview spectra, only faint features from the QW and substrate resonances are resolved. The weak substrate resonance in the reflectivity spectra is highlighted by the dash-dotted ellipse in Fig. 8(a). The energy position of this resonance is essentially independent of θ.

The results of low-temperature reflectivity spectra recorded with increased spectral resolution are depicted in Fig. 8(b) for incidence angles between 26° and 34°. These spectra now also show the resonances of the GaAs substrate (around 1.514 eV) and of the heavy–hole (HH) and light-hole (LH) excitonic resonance of the GaAs QW around 1.54 eV and 1.55 eV, respectively. Within our signal-to-noise ratio, the energy position of the substrate resonance is essentially independent of the angle of incidence. This is to be expected as the substrate layer is buried about 100 nm below the metal interface and thus is only weakly coupled to the strong evanescent field inside the semiconductor.

Both the HH and LH excitonic peaks show a rather pronounced shift of their resonance energies by a few meV when tuning the incidence angle from 26° to 34°. Increasing the incidence angle evidently decreases the detuning between exciton and coupled SPP mode, thereby enhancing the electromagnetic coupling between them. When both modes are energetically brought into resonance by angle tuning, the coherent interaction between the two modes results in the formation of new, coupled exciton–SPP modes with resonance energies which are shifted with respect to the uncoupled exciton mode. As the SPP resonance is highly dispersive, the detuning between SPP and excitonic resonances can be experimentally controlled by varying the angle of incidence. The data in Fig. 8(b) depicts the angle-dependent variation of the HH and LH resonance and reflects the shift between bare exciton and coupled exciton–SPP mode for HH and LH excitons. To our knowledge, these experimental results represent the first clear experimental evidence for a coherent exciton–SPP coupling in hybrid metal–semiconductor nanostructures. A detailed analysis of these results is currently in progress and will be reported elsewhere.

Two preliminary conclusions seem appropriate. First, the coupling which has been observed is of the order of a few meV, similar to the (inhomogeneous) width of the exciton resonance but smaller than the width of the SPP resonance. Therefore these results give evidence for a coherent exciton–SPP coupling, even though a strong coupling regime has not been reached. The model simulations discussed above indicate that a strong coupling between quantum well excitons and SPP may be achieved by further optimization of the grating parameters or by choosing more refined metallic nanostructures. Second, the observa-

tion of exciton–SPP coupling indicates that the coupling to SPP will also affect the radiative damping of the exciton system. Experimental verifications of these effects are currently in progress. We anticipate that similar concepts may be of use for tailoring the radiative damping of other quantum systems, e.g., carbon nanotubes and may result in significant enhancements of the luminescence yield of strongly nonradiatively damped quantum systems.

Acknowledgements The two-photon-induced luminescence experiments have been performed at the Max-Born-Institut in Berlin (Germany) in close collaboration with J. Maultzsch and C. Thomsen from the Technical University of Berlin. We gratefully thank E. Chang, A. Ruini, D. Prezzi and E. Molinari from the INFM National Research Center S3 and the University of Modena, Italy, for the theoretical description of the SWNT spectra. The hybrid metal–semiconductor nanostructures have been fabricated by Yu. I. Mazur, Vas. Kunets and G. G. Salamo at the University of Arkansas (USA) and by P. Srinivasan and E. Johnson at the University of North Carolina (Charlotte, USA) and their important contribution to this work is gratefully acknowledged. We also wish to thank D. S. Kim (Seoul National University), S. Schwieger and E. Runge (TU Ilmenau) for many helpful discussions.

Our work has been financially supported by the Deutsche Forschungsgemeinschaft via the SFB 296. One of us (P.V.) thanks the Alexander von Humboldt Foundation for financial support via a research fellowship. R. P. acknowledges financial support from the Humboldt Graduate School (Berlin).

References

[1] For a recent review see M. S. Dresselhaus, G. Dresselhaus, R. Saito, and A. Jorio, Annu. Rev. Phys. Chem. **58**, 719 (2007).
[2] S. M. Bachilo, M. S. Strano, C. Kittrell, R. H. Hauge, R. E. Smalley, and R. B. Weisman, Science **298**, 2361 (2002).
[3] E. Chang, G. Bussi, A. Ruini, and E. Molinari, Phys. Rev. Lett. **92**, 196401 (2004).
[4] C. D. Spataru, S. Ismail-Beigi, L. X. Benedict, and S. G. Louie, Phys. Rev. Lett. **92**, 077402 (2004).
[5] V. Perebeinos, J. Tersoff, and P. Avouris, Phys. Rev. Lett. **92**, 257402 (2004).
[6] H. Zhao and S. Mazumdar, Phys. Rev. Lett. **93**, 157402 (2004).
[7] C. L. Kane and E. J. Mele, Phys. Rev. Lett. **93**, 197402 (2004).
[8] J. Maultzsch, R. Pomraenke, S. Reich, E. Chang, D. Prezzi, A. Ruini, E. Molinari, M. S. Strano, C. Thomsen, and C. Lienau, Phys. Rev. B **72**, 241402(R) (2005).
[9] Y. Z. Ma, L. Valkunas, S. M. Bachilo, and G. R. Fleming, J. Phys. Chem. B **109**, 15671 (2005).
[10] F. Wang, G. Dukovic, T. F. Heinz, and L. E. Brus, Science **308**, 838 (2005).
[11] G. Dukovic, F. Wang, D. Song, M. Y. Sfeir, T. F. Heinz, and L. E. Brus, Nano Lett. **5**, 2314 (2005).
[12] E. B. Barros, R. B. Capaz, A. Jorio, G. G. Samsonidze, A. G. S. Filho, S. Ismail-Beigi, C. D. Spataru, S. G. Louie, G. Dresselhaus, and M. S. Dresselhaus, Phys. Rev. B **73**, 241406 (2006).
[13] Z. Wang, H. Pedrosa, T. Krauss, and L. Rothberg, Phys. Rev. Lett. **96**, 047403 (2006).
[14] R. B. Capaz, C. D. Spataru, S. Ismail-Beigi, and S. G. Louie, Phys. Rev. B **74**, 121401 (2006).
[15] S. Berger, C. Voisin, G. Cassabois, C. Delalande, P. Roussignol, and X. Marie, Nano Lett. **7**, 398 (2007).
[16] J. Jiang, R. Saito, G. G. Samsonidze, A. Jorio, S. G. Chou, G. Dresselhaus, and M. S. Dresselhaus, Phys. Rev. B **75**, 035407 (2007).
[17] I. B. Mortimer and R. J. Nicholas, Phys. Rev. Lett. **98**, 027404 (2007).
[18] M. Jones, W. K. Metzger, J. McDonald, C. Engtakul, R. J. Ellingson, G. Rumbles, and M. J. Heben, Nano Lett. **7**, 300 (2008).
[19] F. Wang, G. Dukovic, L. E. Brus, and T. F. Heinz, Phys. Rev. Lett. **92**, 177401 (2004).
[20] A. Hagen, G. Moos, V. Talalaev, and T. Hertel, Appl. Phys. A **78**, 1137 (2004).
[21] A. Hagen, M. Steiner, M. B. Raschke, C. Lienau, T. Hertel, H. H. Qian, A. J. Meixner, and A. Hartschuh, Phys. Rev. Lett. **95**, 197401 (2005).
[22] K. Li, M. I. Stockman, and D. J. Bergman, Phys. Rev. Lett. **91**, 227402 (2003).
[23] D. S. Kim, S. C. Hohng, V. Malyarchuk, Y. C. Yoon, Y. H. Ahn, K. J. Yee, J. W. Park, J. Kim, Q. H. Park, and C. Lienau, Phys. Rev. Lett. **91**, 143901 (2003).
[24] M. Damnjanović, I. Milošević, T. Vuković, and R. Sredanović, Phys. Rev. B **60**, 2728 (1999).
[25] R. Pomraenke, J. Maultzsch, S. Reich, E. Chang, D. Prezzi, A. Ruini, E. Molinari, M. S. Strano, C. Thomsen, and C. Lienau, phys. stat. sol. (b) **243**, 2428 (2006).
[26] H. Telg, J. Maultzsch, S. Reich, F. Hennrich, and C. Thomsen, Phys. Rev. Lett. **93**, 177401 (2004).
[27] R. K. Chang and T. E. Furtak, Surface Enhanced Raman Scattering (Plenum Press, New York, 1982).
[28] T. W. Ebbesen, H. J. Lezec, H. F. Ghaemi, T. Thio, and P. A. Wolff, Nature **391**, 667 (1998).
[29] C. Ropers, D. R. Solli, C. P. Schulz, C. Lienau, and T. Elsaesser, Phys. Rev. Lett. **98**, 043907 (2007).
[30] C. Ropers, D. J. Park, G. Stibenz, G. Steinmeyer, J. Kim, D. S. Kim, and C. Lienau, Phys. Rev. Lett. **94**, 113901 (2005).
[31] C. Ropers, G. Stibenz, G. Steinmeyer, R. Müller, D. J. Park, K. G. Lee, J. E. Kihm, J. Kim, Q. H. Park, D. S. Kim, and C. Lienau, Appl. Phys. B **84**, 183 (2006).
[32] J. E. Kihm, Y. C. Yoon, D. J. Park, Y. H. Ahn, C. Ropers, C. Lienau, J. Kim, Q. H. Park, and D. S. Kim, Phys. Rev. B **75**, 035414 (2007).
[33] K. G. Lee and Q. H. Park, Phys. Rev. Lett. **95**, 103902 (2005).
[34] H. Lochbihler, Phys. Rev. B **50**, 4795 (1994).

